

Published in final edited form as:

Chem Mater. 2017 August 8; 29(15): 6279–6288. doi:10.1021/acs.chemmater.7b01367.

Rapid Wafer-Scale Growth of Polycrystalline 2H-MoS₂ by Pulsed Metalorganic Chemical Vapor Deposition

Berc Kalanyan^{*,†}, William A. Kimes[†], Ryan Beams[†], Stephan J. Stranick[†], Elias Garratt[†], Irina Kalish[†], Albert V. Davydov[†], Ravindra K. Kanjolia[‡], and James E. Maslar[†]

[†]Material Measurement Laboratory, National Institute of Standards and Technology, Gaithersburg, Maryland 20899, United States

[‡]EMD Performance Materials, Haverhill, Massachusetts 01835, United States

Abstract

High volume manufacturing of devices based on transition metal dichalcogenide (TMD) ultra-thin films will require deposition techniques that are capable of reproducible wafer-scale growth with monolayer control. To date, TMD growth efforts have largely relied upon sublimation and transport of solid precursors with minimal control over vapor phase flux and gas-phase chemistry, which are critical for scaling up laboratory processes to manufacturing settings. To address these issues, we report a new pulsed metalorganic chemical vapor deposition (MOCVD) route for MoS₂ film growth in a research-grade single-wafer reactor. Using bis(tert-butylimido)-bis(dimethylamido)molybdenum and diethyl disulfide we deposit MoS₂ films from ≈ 1 nm to ≈ 25 nm in thickness on SiO₂/Si substrates. We show that layered 2H-MoS₂ can be produced at comparatively low reaction temperatures of 591 °C at short deposition times, approximately 90 s for few-layer films. In addition to the growth studies performed on SiO₂/Si, films with wafer-level uniformity are demonstrated on 50 mm quartz wafers. Process chemistry and impurity incorporation from precursors are also discussed. This low-temperature and fast process highlights the opportunities presented by metalorganic reagents in the controlled synthesis of TMDs.

Keywords

MoS₂; MOCVD; CVD; transition metal dichalcogenides; metalorganic chemistry

1. INTRODUCTION

Layered two-dimensional (2D) transition-metal dichalcogenides (TMDs), *e.g.*, MoS₂, WSe₂, ReS₂, are of increasing interest for next-generation nanoelectronic and optoelectronic devices due to their unique thickness modulated electronic properties¹. When structured into

^{*}Corresponding Author: berc.kalanyan@nist.gov.

Notes

The authors declare no competing financial interest.

Supporting Information Available

Dependence of film crystallinity on substrate temperature, AFM and SEM images, XPS spectra of early nucleation, XPS depth profile and survey scans, thickness uniformity on quartz wafers. This material is available free of charge via the Internet at <http://pubs.acs.org>.

single or few atomic layers, some TMDs develop a direct band gap due to quantum confinement², which enables their use in low-power field effect transistor (FET) devices^{3–5}. In addition to traditional logic devices, structures consisting of TMDs are also being investigated for use in valleytronics⁶, memory applications⁷, chemical sensing^{8,9}, optoelectronics^{10–12}, energy devices¹³, and life sciences^{14,15}. When assembled into van der Waals heterostructures with TMDs or other 2D materials (*e.g.*, graphene, hexagonal BN, *etc.*) novel and unique device arrangements^{16,17} become realizable without the need for epitaxial matching between the layers. Furthermore, incorporation of dopants into TMDs^{18–21}, alloying of various layered compounds²², and heterojunction assemblies^{23–25} highlight the immense level of tunability afforded by layered 2D systems. Despite their tremendous potential for new applications, synthetic routes available for 2D TMDs have been largely limited to growth techniques that are difficult to scale, have low throughput, or do not offer sufficient control over the process chemistry to achieve reproducible material properties. Additionally, commonly employed powder vaporization routes, *e.g.*, MoS₂ from MoO₃ and S, require high growth temperatures and are not suitable for downstream integration with existing electronic manufacturing process flows.

Synthetic high-quality bulk TMD crystals are commonly produced using the chemical vapor transport method²⁶. After growth, individual layers held together by van der Waals forces can be separated from the bulk by mechanical exfoliation and transferred onto device substrates. Although this approach is successful for small scale device development and fundamental studies, large-area growth of TMDs requires vapor-phase deposition routes. The simplest approach that employs vapor-phase reagents is direct chalcogenization of metal foils^{27,28} or thin films²⁹. These approaches pose several challenges, particularly in terms of compatibility with semiconductor process flows and 3D integration. For instance, growth on sacrificial substrates requires the mechanical transfer of TMDs onto a target substrate and metal chalcogenization requires a separate metal deposition step. Among other growth techniques, powder vaporization in flow tube reactors using inorganic sources such as transition metal oxides and elemental chalcogens have been widely used to produce a variety of 2D TMDs^{30–34}. While high-quality films are routinely produced in this manner, the inherent lack of control over precursor flux and process variability associated with the flow tube geometry severely limit the scalability of powder vaporization. Even with high vapor pressure precursors, hot-walled flow tube reactors present problems with parasitic wall reactions, *i.e.*, partial conversion of precursors before they reach the substrate.

To overcome scalability and process control issues, recent reports on TMD synthesis have focused on using alternative metal precursors, primarily transition metal halides³⁵ such as MoCl₅ or metal carbonyls³⁶ such as Mo(CO)₆. Halides have also been used in low-temperature processes, with several examples of atomic layer deposition (ALD)^{37,38} reported to date. At low growth temperatures, ALD TMD routes do not produce crystalline material and corrosive reaction products are generally undesirable. Recently, a new CVD route was proposed by Robinson *et al.*³⁹ using W(CO)₆, (CH₃)₂Se, and H₂, to produce large-grain WSe₂. Using an analogous chemistry, Kang *et al.*³⁶ found that layer-by-layer or 2D growth of MoS₂ occurred in a tube reactor under sufficiently low Mo(CO)₆ flux, which necessitated extremely long growth times of 26 hours per monolayer MoS₂. Metal carbonyls are typically used for low-temperature metal CVD reactions due to their zerovalent state⁴⁰.

However, high reaction temperatures (typically 800 °C to 900 °C) needed to produce large grain TMDs pose unique challenges for transition metal carbonyl sources. Iron and nickel carbonyls are known to form⁴¹ readily upon reaction of CO and H₂ with exposed stainless steel surfaces (*e.g.*, reactor walls). These conditions are met in CVD reactions that liberate CO from metal carbonyls and often employ H₂ as a reducing agent. *In situ* formation of Fe and Ni carbonyls could become a source of downstream Fe and Ni contamination for metal carbonyl based chemical vapor deposition (CVD) routes. In contrast to the inorganic⁴² metal sources in use today, metalorganic precursors are expected to offer greater flexibility and a higher degree of controllability for processing in conventional CVD reactor hardware.

In this article we report a new MOCVD process that addresses some of the challenges encountered in the state of the art vapor-phase TMD growth. Here, we present a new MOCVD process that uses metalorganic and organosulfur precursors and produces wafer-scale 2H-MoS₂ films at short deposition times from tens of seconds to several minutes. We use a pulsed injection strategy to discretize the growth process, which, to our knowledge, is the first reported pulsed MOCVD process for 2D TMD growth. The relatively low growth temperature of 591 °C employed in this work makes our process thermally compatible with a variety of substrates, including flexible glasses used in consumer electronics⁴³. Through extensive post-deposition characterization, we relate film properties to process conditions. We show that few-layer MoS₂ can be readily produced on 50 mm diameter substrates, with sub-monolayer control over aggregate film thickness. Chemical analyses show impurity incorporation and ligand removal steps, which suggests that precursor chemistry impacts the film deposition process and that exploration of additional metalorganic precursors may provide new vapor-phase synthetic routes for TMD growth.

2. EXPERIMENTAL METHODS

a. Surface preparation

Surfaces used for growth characterization consisted of 90 nm thermal SiO₂ on Si(100). For each growth run, 32 mm × 32 mm coupons were cleaved from a 300 mm wafer and degreased using acetone and methanol, and subsequently dried using a stream of nitrogen. X-ray photoelectron spectra from as-cleaned substrates showed only Si, O, and C species, the latter being ascribed to adventitious carbon.

b. MOCVD growth

Films were grown in a single-wafer perpendicular flow reactor described elsewhere⁴⁴. Briefly, the reactor consisted of a resistively heated thin-walled stainless steel pedestal, independently heated aluminum walls, and o-ring sealed flanges. Gas flow direction was normal to the plane of the receiving substrate. Walls were maintained at 160 °C and upstream lines were heated to prevent precursor condensation. Substrates were placed on the steel pedestal and heated to a surface temperature of approximately 591 °C ± 1 °C, measured using a type-K thin-wire thermocouple embedded on a test wafer. Substrates were allowed to thermally equilibrate for 10 minutes once the heater setpoint was reached. Reactions were run at 160 Pa using 400 mL/min (standard cubic centimeters per minute, SCCM) of argon (99.999 %) at standard temperature and pressure (STP) with the carrier gas distributed

among four delivery lines. Here, STP is defined as 0 °C and 101.33 kPa. The reactor was pumped using a twin-screw pump with an ultimate pressure of approximately 0.01 Pa. The metal precursor was electronic grade bis(tert-butylimido)-bis(dimethylamido)molybdenum, $(\text{N}^t\text{Bu})_2(\text{NMe}_2)_2\text{Mo}$, installed in a 300 mL stainless steel ampoule, heated to 28 °C in an oven, and delivered by flowing 25 SCCM of carrier gas over the ampoule head space (vapor draw). Electronic grade diethyl disulfide (Et_2S_2 , >98 %) was used as the sulfur source and was delivered out of a 100 mL single-port ampoule heated to 60 °C. Carrier flow rate in the Et_2S_2 line was 100 SCCM, with two auxiliary lines delivering the balance. In order to limit the amount of Et_2S_2 delivered, a 250 μm diameter steel orifice was installed between the ampoule and the injection valve. After deposition, the wafer heater was allowed to cool to ≈ 160 °C, at which point the reactor was back filled with Ar and the wafer immediately removed and placed on a cold surface. As a result of this procedure, all deposited films were briefly exposed to laboratory ambient at ≈ 160 °C upon removal from the reactor.

Each reaction cycle consisted of 1.5 s long co-injections of $(\text{N}^t\text{Bu})_2(\text{NMe}_2)_2\text{Mo}$ centered on 2.0 s long injections of Et_2S_2 . Pulse duration for the Et_2S_2 was kept slightly longer than the Mo source in order to preclude reactions of $(\text{N}^t\text{Bu})_2(\text{NMe}_2)_2\text{Mo}$ in the absence of sulfur. After each co-injection of Mo and S reagents, the reactor was purged with 400 SCCM of Ar for 4.0 s, resulting in a 6.0 s cycle time. A graphical representation of the reaction chamber and the pulse valve timing scheme are shown in Figure 1. High precision pulse timing and repeatability was incorporated into the injection system using low-jitter digital delay generators. In this fashion, reaction cycles were iterated n number of times to vary the thicknesses of MoS_2 deposited. For example, we will write $n=15$ to mean 15 injections of $((\text{N}^t\text{Bu})_2(\text{NMe}_2)_2\text{Mo} + \text{Et}_2\text{S}_2)$. By employing pulsed injections, we effectively regulated the amount of material delivered to the growth surface and arbitrarily discretized the time coordinate of the growth process.

c. Characterization

Raman and photoluminescence (PL) spectra were obtained with 532 nm excitation in a back-scattering configuration using a custom-built Raman microprobe system. The incident laser was spatially filtered and sent into the microscope after passing through a linear polarizer to define the excitation polarization. Radiation was introduced into the microscope optical path using an angled dielectric edge filter in an injection-rejection configuration. A 40 \times , 0.75 numerical aperture infinity-corrected microscope objective was used for focusing incident radiation and collecting scattered/emitted radiation. Power levels at the sample were less than about 1 mW and 0.1 mW for Raman and photoluminescence spectroscopy, respectively. Collected scattered/emitted radiation was coupled to a multimode optical fiber and delivered to a 0.5 m focal length and 0.3 m focal length imaging, single spectrograph for Raman and photoluminescence spectroscopy, respectively. Light was detected with a back-illuminated, charge coupled device (CCD) camera system operating at -70 °C and -75 °C for the Raman and PL CCD cameras, respectively. The instrumental bandpass full width at half maximum (FWHM) was approximately 2.2 cm^{-1} at 347 cm^{-1} and 18.3 cm^{-1} at 1700 cm^{-1} for Raman and photoluminescence spectroscopy, respectively. Laser wavelength was determined using a commercial wavemeter.

Cross sectioning for high resolution transmission electron microscopy (HRTEM) was performed using an FEI Nova Nanolab instrument (FEI Company, Hillsboro, OR). To protect sample integrity, thin layers of C (10 nm) and Pt (250 nm) were deposited using an electron beam operating at 5 keV. The final Pt cap was deposited using the ion beam operating at 30 keV. Samples were extracted and thinned using standard lift-out techniques. HRTEM was performed using an FEI Titan 80-300 AEM (FEI Company, Hillsboro, OR). Images were obtained with a multi-scan CCD camera with a single 1024×1024 pixel detector using 300 keV electrons through a 60 μm aperture at 1 nA of current for 1 s acquisition times. Sample thickness was nominally 100 nm or less for all images obtained. Fourier transformations were calculated using Gatan DigitalMicrograph (v3.10) (Gatan Inc., Pleasanton, CA).

X-ray photoelectron spectroscopy (XPS) was carried out using a Kratos Axis Ultra DLD instrument from Kratos Analytical (Chestnut Ridge, NY), which incorporated a monochromated Al Kα source operated at 104 W (8 mA; 13 kV) and a hemispherical analyzer. Spectra were acquired at an analyzer pass energy of 40 eV and the analysis area was approximately 1 mm by 0.5 mm. Spectra were charge calibrated against S 2p_{3/2} (S-Mo, 162.0 eV) assigned to MoS₂⁴⁵. A low energy electron gun was used for charge neutralization. Elemental percentages were calculated by taking the average of at least three non-overlapping measurements, with the uncertainty given as ± one standard deviation of the mean. Film thickness was estimated based on the inelastic scattering of Si 2p photoelectrons by an MoS₂ overlayer. The inelastic mean free path (IMFP) for Si 2p at a kinetic energy of 1383 eV was estimated to be 2.537 nm using the TPP-2M formula as implemented in the NIST Electron Inelastic-Mean-Free-Path Database⁴⁶. Parameters used for the IMFP calculation were $\rho_{\text{MoS}_2} = 5.06 \text{ g} \cdot \text{cm}^{-3}$ (for bulk molybdenite⁴⁷), $E_{g, \text{MoS}_2} = 1.8 \text{ eV}$ (monolayer²), and 18 valence electrons, where ρ is the mass density and E_g is the band gap. Peak fitting was done using the CasaXPS software package (v2.3.17) (Teignmouth, U.K.). Sputter depth profiling was done using 4 keV Ar⁺ ions delivered to the surface at a 70° angle of incidence. The ion beam was rastered over an area of 3 mm × 3 mm at a current density of approximately 0.5 mA/cm². The analysis area was within the plateau of the sputter crater.

X-ray diffraction (XRD) data were collected using a conventional powder diffractometer by Phillips in the θ - 2θ configuration using CuKα radiation ($\lambda = 0.15418 \text{ nm}$). The XRD scans were analyzed using the MDI-JADE 6.5 software package (Jade 6.5, Materials Data, Inc. Livermore, CA., 2015). MoS₂ c-lattice parameter was calculated by cell refinement. Complimentary two-dimensional X-ray diffraction (XRD^2) patterns were collected on a Bruker-AXS D8 Discover diffractometer (Bruker Corporation, Billerica, MA), equipped with an area detector (Hi-star), using CuKα radiation. Intensity of the 0002 reflection from the XRD^2 pattern was angle-integrated along the χ direction, which is equivalent to sample tilting in a conventional diffractometer, to produce a “rocking curve”-like plot (see inset in Figure 6) to assess the degree of texture in the film. The angle integrated patterns were examined using Bruker AXS Ddifracplus EVA software.

Atomic force microscope (AFM) topographic images were collected using an Asylum Research MFP-3D instrument (Asylum Research, Goleta, CA). The measurements were done in tapping mode using a stiff cantilever (Si, 42 N/m) with a large driving amplitude and setpoint. Surface roughness values are calculated as the root mean square (RMS) of the height data.

Scanning electron microscopy (SEM) characterization was done using Hitachi S-4700 (Hitachi High-Technologies Europe GmbH, Krefeld, Germany) and JEOL JSM-7100 (JEOL Ltd., Tokyo, Japan) field emission instruments operated at 20 kV accelerating voltage with the sample stage tilted to 70° in order to assess the film's morphology.

3. RESULTS AND DISCUSSION

Films were grown on wafer substrates using pulsed injections of $(\text{N}^t\text{Bu})_2(\text{NMe}_2)_2\text{Mo}$ and Et_2S_2 as described in the Experimental section. We varied the number of pulses to scale the thickness of the MoS_2 films deposited. The flow distribution in this reactor geometry has been previously modeled⁴⁴ using computational fluid dynamics and results in visually uniform coatings on large-area substrates. To demonstrate uniform and large-area deposition of MoS_2 , we grew films of various thicknesses on 50 mm diameter fused quartz wafers. Photographs of wafers with $n=0, 15, 50,$ and 100 injections of $(\text{N}^t\text{Bu})_2(\text{NMe}_2)_2\text{Mo}$ and Et_2S_2 are shown in Figure 1 (b). The coatings are uniform to the eye over the diameter of the wafers and show decreasing optical transmission with increasing film thickness.

Few-layer MoS_2 films were grown and subsequently characterized using cross-sectional HRTEM, Raman spectroscopy, PL spectroscopy, XRD, and XPS. We found that growth on thermal SiO_2 exhibited gross inhomogeneities at $n < 10$, associated with nucleation or incomplete surface coverage. In order to characterize the properties of coalesced and continuous films, we focused our attention on films growth with 25 pulses. Cross-sectional HRTEM images from a film deposited using $n=25$ are shown in Figure 3 (a) through (c). In Figure 3 (a), MoS_2 can be identified by the dark contrast between the SiO_2 layer and the protective carbon coating. The film is continuous within the field of view, with some areas showing non-uniformities in thickness. Regions of the film that appear to be out of focus may be a result of sample preparation. These regions could be the topmost MoS_2 sheet that has come loose during cross sectioning and is projecting away from the plane of the image. The higher magnification image in Figure 3 (b) is from the dashed area in Figure 3 (a). Here, a layered structure is clearly discernable, with some layers exhibiting non-planar stacking. A higher magnification view in Figure 3 (c) shows approximately 6 layers present with a total thickness of $4.08 \text{ nm} \pm 0.20 \text{ nm}$, taken as the average of ten line measurements in Figure 3 (b). Interplane spacing was measured to be $0.68 \text{ nm} \pm 0.05 \text{ nm}$, in agreement with the expected separation between stacked MoS_2 layers⁴⁸.

The orientation of the first few MoS_2 layers with respect to the amorphous substrate may give some insights into the initial nucleation mechanism. Several layers in Figure 3 (b) emerge from the substrate and terminate back at the substrate a short distance away, *ca.* 10 nm. Second, third, and subsequent MoS_2 planes show significantly longer continuity, with some layers extending beyond 50 nm without interruption. Also in Figure 3 (b), some

regions of the image show branching and merging MoS₂ planes. One growth model that would account for these observations is island nucleation. In this model, the anchor points at which the MoS₂ originates out of the substrate could be the initial nucleation sites. Surface-limited reaction of (N^tBu)₂(NMe₂)₂Mo with hydroxyl groups was reported for ALD of MoO₃⁴⁹ and MoN^{50,51} at <325 °C. Assuming a similar interaction with surface hydroxyls, the initial formation of Si-O-Mo bonds may also play a role in MoS₂ nucleation. Accordingly, the formation of the first MoS₂ layer may be influenced by the substrate chemistry, whereas subsequent layers could form based on interactions with existing MoS₂ surfaces. Differences in layer continuity between the first and subsequent MoS₂ layers gives some validity to this distinction. Since the reaction temperatures in this study are low (<600 °C) relative to furnace grown TMDs, the Mo adatoms are expected to have limited surface mobility and, therefore, rearrangements at the MoS₂/SiO₂ interface are less likely. Under such conditions, grain size could be dependent on the initial nucleation process. The interface shown in Figure 3 (b) and (c) is remarkably similar to that produced by pulsed laser deposition (PLD)⁵² at 700 °C, showing that surface rearrangement may not be favorable even at higher substrate temperatures for fast deposition processes. While we focused this work on wafer-scale growth and pulse modulated thickness control, deposition at a higher reaction temperature and on crystalline substrates is expected to promote better long range ordering of MoS₂ basal planes. Further discussion of growth temperature is provided in the Supporting Information (Figure S1).

In addition to comparatively low deposition temperatures afforded by this MOCVD chemistry, controlled and reproducible growth of TMDs is also highly desirable. By employing pulsed injections of precursor, we can impose digital control over film thickness, which is otherwise difficult to achieve with a continuous deposition process. Although a continuous process could have been used, we implemented pulsed injections to mitigate transient effects associated with the depletion of precursor vapor in a vapor draw configuration, as employed in this work. To illustrate thickness scaling that is achievable by our pulsed MOCVD scheme, we systematically varied the number of (N^tBu)₂(NMe₂)₂Mo and Et₂S₂ injections at a wafer temperature of 591 °C and studied the resultant films by XPS. By measuring the attenuation of the Si 2p photoelectrons originating in the SiO₂ layer, we were able to estimate the average thickness of the MoS₂ overlayer over the sampled area (see Supplemental Information for details). Given the large analysis area of XPS (≈ 0.5 mm²) compared to the MoS₂ crystallite size, film thicknesses calculated from XPS are representative of the amount of material on the surface without accounting for the growth mode. Figure 4 (a) shows the results of this analysis. We found that film thickness increases linearly with *n* and the MOCVD process gives rise to Mo 3d signal after a single injection of the reactants (Figure S2). Since the reactivity of (N^tBu)₂(NMe₂)₂Mo with hydroxylated surfaces is known, the lack of a chemisorption delay is not surprising. Interestingly, the thickness intercept in Figure 4 (a) is non-zero, which could indicate the presence of an interfacial layer that develops during nucleation or a surface contamination layer that exists prior to deposition. These would be reasonable possibilities since the substrates do not undergo *in situ* cleaning before growth. While the origin of this offset is not clear, the linear trend in Figure 4 (a) demonstrates the level of thickness control afforded by the pulsed injection strategy. The aggregate growth rate is determined to be 0.12 nm/pulse, which is

equivalent to < 1 ML of MoS₂ deposited per injection, when considered on a planar basis. Given that 2H-MoS₂ is a layered crystal with a fixed d spacing, an aggregate growth rate less than d suggests that surface coverage is less than unity per pulse. The aggregate thickness control achieved using our MOCVD approach demonstrates that a pulsed-metering of the precursor delivered to the substrate can provide fine control over film thickness for a fast TMD deposition process. For further analysis of the way in which growth proceeds we turn to AFM.

Figure 4 (b) shows the evolution of surface roughness for the same range of thicknesses analyzed by XPS. For $n = 15$, film roughness remains below 2 nm. Within this regime, films are relatively smooth and exhibit a uniform distribution of small features < 20 nm in lateral dimensions, as shown in Figure S3. At $n=25$, roughness increases to 2.4 nm, and continues to rise, reaching 6 nm at $n=50$. Despite the large roughness factor, all MoS₂ on the surface is accounted for by XPS since Si 2p photoelectrons have a finite escape probability through an MoS₂ layer up to ≈ 8 nm thick. Contrasting the linear growth rate measured by XPS to the onset of surface roughening at $n=25$, we postulate that 3D or out-of-plane MoS₂ growth takes place beyond ≈ 4 nm of growth. Indeed, we find that beyond 50 pulses, films continue to roughen. Accompanying SEM images show that the rough areas evident at $n=25$ take the form of randomly oriented features by $n=50$, and eventually grow into sharp platelets emerging from the surface at $n=100$ (Figure S4). Additional deposition ($n=200$) produces a continuous surface with rounded features. One potential explanation for this evolution in film morphology is a growth process with a distinct nucleation phase. At $n = 15$ the growth could be dominated by precursor-substrate interactions, as the initial few ML of MoS₂ are formed. Subsequent deposition of MoS₂ on existing MoS₂ sites includes a 3D growth component, where out-of-plane crystallites can form alongside the layered structure confirmed by TEM and diffraction measurements (discussed below).

The complex evolution of MoS₂ layering, surface coverage, and morphology is a confounding factor for spectroscopic measurements. For this reason we will limit spectroscopic analyses to few-layer MoS₂ to confirm optical and optoelectronic characteristics. We found that PL yield for our MoS₂ films was maximized around $n=15$, therefore we focused subsequent analysis on few-layer material produced with 15 pulses.

The Raman spectrum in Figure 5 (a) exhibits in-plane (E_{2g}^1) and out-of-plane (A_{1g}) modes associated with 2H-MoS₂ at 384.7 cm^{-1} and 407.2 cm^{-1} , respectively. The broad asymmetric feature at 454 cm^{-1} has been ascribed to a superposition of second-order zone-edge phonon $2LA(M)$ and the first-order optical phonon A_{2u}^{53} . These modes were previously observed in bilayer MoS₂ from natural crystals. While the position and the separation of E_{2g}^1 and A_{1g} are oftentimes correlated with the number of MoS₂ layers^{53,54}, quantitative relationships have only been established for exfoliated single crystal materials. Since line positions are influenced by the local electronic environment, an exact determination of film thickness for CVD films is complicated by factors such as local inhomogeneities (*e.g.*, simultaneous sampling of multiple grains), rotational stacking faults, and grain size⁵⁵. For these reasons, we rely on XPS and HRTEM for thickness measurements as described earlier.

To further assess the optoelectronic properties of our MOCVD films, we turn to photoluminescence (PL) spectroscopy. PL can often complement Raman spectroscopy, since large differences in PL yield can help discriminate between monolayer (ML) and few-layer MoS₂. The PL spectrum of the same surface from Figure 5 (a) is shown in panel (b). The two broad features centered at 2.04 eV (656.0 nm) and 1.89 eV (607.6 nm) are assigned to the A and B excitons, respectively, originating from the direct gap transition at the K point. The energy of the A and B excitons are consistent with measurements from natural MoS₂ samples, and the simultaneous presence of the two transitions generally suggests a multi-layer film^{2,56,57}. As with Raman, existing literature on PL of MoS₂ focuses on single-crystal measurements. Since our MOCVD films are polycrystalline and likely comprise an ensemble of layers (*i.e.* a mixture of different layer numbers), a reliable determination of thickness or layer number is left to other measurements.

Chemical analysis by XPS of the same films produced with $n=15$ is shown in Figure 5 (c) and (d). The high resolution spectrum in Figure 5 (c) shows Mo 3d and S 2s core-levels. Two types of Mo species are apparent due to the presence of two Mo 3d doublets. The lower binding energy (B.E.) doublet is ascribed to MoS₂, with the 3d_{5/2} and 3d_{3/2} spin-orbit components positioned at 229.1 eV and 232.3 eV ($\Delta = 3.15$ eV), respectively, comparable to values reported for natural MoS₂ crystals⁴⁵. Oxidized Mo is observed as a higher B.E. doublet at 232.3 eV and 235.5 eV, likely from the oxidation of unsaturated Mo sites upon exposure to air. This thin oxide layer is typically described as MoO₃ and is known to develop⁵⁸ over time on both natural and synthetic MoS₂. A broad S 2s transition is found at 226.4 eV, as expected for MoS₂. Looking at the corresponding S 2p transition in (d), only one species of S is apparent, with the position of the S 2p doublet (162.2 eV and 163.3 eV) consistent with S-Mo bonding in MoS₂. The presence of the Si 2s peak at 154.8 eV confirms that the MoS₂ film is thin enough to transmit photoelectrons from the underlying SiO₂/Si substrate (<8 nm). The main impurity found in the films is graphitic carbon, which will be discussed in more detail below.

To investigate the crystal structure of the MOCVD films, we grew ≈ 25 nm thick MoS₂ using 200 pulses of Mo and S precursors and analyzed the XRD patterns generated therefrom. The XRD pattern in Figure 6 was obtained by measuring a θ -2 θ scan from such a film. The as-grown film is crystallized into the single phase 2H-MoS₂ hexagonal polytype with space group $P6_3/mmc$ (D_{6h}^4 in Schönflies notation, or #194 in ITC⁵⁹). In agreement with the layered structure apparent in the HRTEM images, strong (000 l) texturing in the 2 θ scan indicates c-plane oriented growth. Refined lattice parameter $c = 1.2306(5)$ nm was obtained using PDF #01-073-1508 (ICCD, 2010) and is consistent with values reported in the

literature^{60,61}. Plane spacing of $d = \frac{c}{2} = 0.612$ nm was also in excellent agreement with values reported elsewhere⁶². Since the XRD patterns were obtained from thick MoS₂ specimens ($n=200$, ≈ 25 nm), reasonable agreement between the calculated d and HRTEM layer spacing for few-layer MoS₂ ($n=25$) indicates that a considerable degree of crystallinity persists even for thick MoS₂ films. The relatively narrow rocking curve shown in the inset to Figure 6 is further evidence to the high level of texturing in the MOCVD films.

To assess the bulk composition and stoichiometry of our MOCVD grown material, we used the same ≈ 25 nm thick MoS_2 film ($n=200$) for XPS analysis. The main impurity in the film was found to be carbon, which is discussed in more detail below. We found that C accumulation in the film was correlated with the number of pulses used to grow the film. To exclude contributions from adventitious hydrocarbons, we sputtered the MoS_2 surface prior to compositional analysis. The depth profile obtained from this analysis is shown in the Supporting Information (Figure S5). Elemental impurities left in the film after 60 s of Ar^+ sputtering were carbon (5%) and oxygen (5%). The true internal composition of the film could not be measured by XPS, as longer ion milling suffers from preferential sputtering of sulfur⁶³. Film stoichiometry near the surface was determined to be $\text{S}:\text{Mo} = 1.95 \pm 0.01$ as calculated from the Mo 3d and S 2p core levels. A small degree of sulfur deficiency due to undercoordinated Mo edge sites has also been noted for other synthetic MoS_2 films and is likewise encountered in natural single crystals⁶⁴.

In addition to process characteristics and optoelectronic properties, we also evaluated the growth chemistry of our MOCVD process. To assess the role of each precursor in the deposition process, we grew thick films at 591 °C with and without a sulfur source and compared the binding state of Mo, N, C, and S core electrons. Photoelectron spectra from these films are shown in Figure 7, where the lower spectra (black) represent films grown using $(\text{N}^t\text{Bu})_2(\text{NMe}_2)_2\text{Mo}$ alone and the upper spectra (blue) denote those grown using the Mo source together with Et_2S_2 . The Mo 3p region for the surface exposed to sulfur, in panel (a), shows evidence for a single Mo species that dominates the spectrum. Here, the doublet at 395.0 eV and 412.5 eV satisfies the 2:1 area ratio for spin-orbit splitting and is ascribed to MoS_2 . The broad feature at 417.4 eV is likely a surface plasmon peak, also observed in pristine MoS_2 specimens⁴⁵. While a small MoO_3 component can be discerned in the spectrum, this contribution is more readily evident in the Mo 3d region. Looking at the spectrum from a surface exposed to the Mo precursor only (lower trace), two doublets are clearly resolved. However, the doublets alone do not fully account for the Mo 3p core spectrum, since the relative intensity relationship between the $3p_{3/2}$ and $3p_{1/2}$ peaks requires the presence of an additional component at 397.8 eV. This peak corresponds to the N 1s transition, likely a result of N-Mo bonding. The presence of the N KLL Auger transition in the survey spectrum further corroborates this hypothesis (Figure S6). The position of the lower B.E. Mo $3p_{3/2}$ component is consistent with either a sulfide or a nitride species. We discount the possibility of metallic Mo since Mo^0 would be expected at a lower binding energy. Indeed, the Mo 3d and S 2s regions in Figure 7 (c) clearly indicate the presence of MoS_2 when Et_2S_2 is used in the reaction, and show oxidized Mo in addition to the lower B.E. doublet when the reaction is run without Et_2S_2 . The relatively large contribution from MoO_3 in the Mo-only film indicates that a significant fraction of the deposited film consists of unsaturated Mo (possibly metallic) that is subsequently oxidized upon removal from the reactor (≈ 160 °C). The position of the lower B.E. Mo 3d doublet is consistent with either MoS_2 or Mo_xN_y , but the relative absence of sulfur (< 3 %, from residual sulfur in the reactor) and the detection of N 1s favors the latter possibility. The peak shape of the Mo $3d_{5/2}$ transition at 228.9 eV is also consistent with Mo nitride, which is known to produce asymmetric peak shapes since MoN is a good electrical conductor⁶⁵.

The interpretation of the Mo regions is corroborated by the C 1s spectra, shown in Figure 7 (b). For the films grown with and without a sulfur source, the salient differences in the C 1s region are the absence and presence of oxidized carbon species. For the surface exposed to Et₂S₂, the C 1s region shows a single asymmetric peak at 284.2 eV, which is ascribed to graphitic carbon due to its unique asymmetric peak shape⁶⁶. In contrast, the surface that was only exposed to the Mo precursor produces a C 1s spectrum with two additional peaks at 286.6 eV and 288.6 eV. The former peak most likely stems from C-O bonding, with the latter peak position being high enough in B.E. to denote C=O or C-N. Since the Mo and S precursors do not possess any oxygen-containing functionality, the incorporation of O into the films is largely a result of atmospheric exposure, although a low background of oxygen in the reactor cannot be excluded. The notable absence of distinct C-O or C=O related peaks in the Et₂S₂-exposed surface makes it unlikely that adventitious carbon is the source of these oxygen-containing groups. A plausible explanation of the spectra is the generation of C-O and C=O functionality on the film surface upon expose to air, possibly by oxidation of unreacted ligands on the surface. This suggests that a ligand removal mechanism may play a part in the deposition process and Et₂S₂ is not simply a source of sulfur atoms, but rather a reactant that interacts with the growth surface or the metal precursor in the thermal boundary layer. This hypothesis is further supported by the observation that residual nitrogen remains in the films when the sulfur source is omitted, but N-containing ligands (amides and imides) are absent when Et₂S₂ is used during growth. Therefore, the chemistry behind our MOCVD MoS₂ growth is not a simple case of Mo⁰ deposition followed by sulfurization. This apparent interaction between precursor ligands is also distinct from processes that use Mo(CO)₆, which thermally decomposes⁶⁷ into Mo⁰ and can be subsequently sulfurized⁶⁸. Since reaction chemistry plays a part in growth, our MOCVD process highlights the opportunities in new precursor design and reaction schemes for scalable and controllable TMD growth processes.

4. CONCLUSION

Large area and controllable growth of TMDs require reaction chemistries that are compatible with industrially relevant growth techniques such as MOCVD. We have presented process characteristics and film properties for wafer-scale growth of 2H-MoS₂ using metalorganic and organosulfur reagents in a pulsed MOCVD reactor. Polycrystalline few-layer films were produced at comparatively low temperatures (<600 °C) with fast deposition times on the order of seconds to minutes. Pulsed injections of precursor vapors facilitated excellent control over film thickness, producing films of <1 nm to 25 nm in thickness, with a growth rate of 0.12 nm/pulse. Our process demonstrates the feasibility of using low vapor pressure metalorganic sources as reagents for TMD growth and presents a viable alternative to various inorganic sources used up to this point. Moreover, the large library of metalorganic compounds offer process designers the flexibility in choosing reagents based on volatility, thermal stability, and reactivity. While the temperature of our process imposes limitations on TMD grain size, low temperature and fast processing could be advantageous for applications requiring thermal compatibility with flexible glass substrates and low cycle times for roll-to-roll processing.

Supplementary Material

Refer to Web version on PubMed Central for supplementary material.

Acknowledgments

We would like to thank SUNY Poly SEMATECH (formerly SEMATECH) for providing diethyl disulfide (Air Products) and EMD Performance Materials for supplying the $(\text{N}^t\text{Bu})_2(\text{NMe}_2)_2\text{Mo}$ precursor.

Certain commercial equipment, instruments, and materials are identified in this publication to adequately specify the experimental procedure. Such identification in no way implies approval, recommendation, or endorsement by the National Institute of Standards and Technology, nor does it imply that the equipment, instruments, or materials identified are necessarily the best available for the purpose.

References

1. Mak KF, Shan J. Photonics and Optoelectronics of 2D Semiconductor Transition Metal Dichalcogenides. *Nat Photonics*. 2016; 10:216–226.
2. Mak KF, Lee C, Hone J, Shan J, Heinz TF. Atomically Thin MoS_2 : A New Direct-Gap Semiconductor. *Phys Rev Lett*. 2010; 105:136805. [PubMed: 21230799]
3. Radisavljevic B, Radenovic A, Brivio J, Giacometti V, Kis A. Single-Layer MoS_2 Transistors. *Nat Nanotechnol*. 2011; 6:147–150. [PubMed: 21278752]
4. Kim S, Konar A, Hwang W-S, Lee JH, Lee J, Yang J, Jung C, Kim H, Yoo J-B, Choi J-Y, et al. High-Mobility and Low-Power Thin-Film Transistors Based on Multilayer MoS_2 Crystals. *Nat Commun*. 2012; 3:1011. [PubMed: 22910357]
5. Sarkar D, Xie X, Liu W, Cao W, Kang J, Gong Y, Kraemer S, Ajayan PM, Banerjee K. A Subthermionic Tunnel Field-Effect Transistor with an Atomically Thin Channel. *Nature*. 2015; 526:91–95. [PubMed: 26432247]
6. Mak KF, He K, Shan J, Heinz TF. Control of Valley Polarization in Monolayer MoS_2 by Optical Helicity. *Nat Nanotechnol*. 2012; 7:494–498. [PubMed: 22706698]
7. Cheng P, Sun K, Hu YH. Memristive Behavior and Ideal Memristor of 1T Phase MoS_2 Nanosheets. *Nano Lett*. 2016; 16:572–576. [PubMed: 26654683]
8. Liu B, Chen L, Liu G, Abbas AN, Fathi M, Zhou C. High-Performance Chemical Sensing Using Schottky-Contacted Chemical Vapor Deposition Grown Monolayer MoS_2 Transistors. *ACS Nano*. 2014; 8:5304–5314. [PubMed: 24749814]
9. Roy K, Padmanabhan M, Goswami S, Sai TP, Ramalingam G, Raghavan S, Ghosh A. Graphene- MoS_2 Hybrid Structures for Multifunctional Photoresponsive Memory Devices. *Nat Nanotechnol*. 2013; 8:826–830. [PubMed: 24141541]
10. Ross JS, Klement P, Jones AM, Ghimire NJ, Yan J, Mandrus DG, Taniguchi T, Watanabe K, Kitamura K, Yao W, et al. Electrically Tunable Excitonic Light-Emitting Diodes Based on Monolayer WSe_2 P-N Junctions. *Nat Nanotechnol*. 2014; 9:268–272. [PubMed: 24608230]
11. De Fazio D, Goykhman I, Yoon D, Bruna M, Eiden A, Milana S, Sassi U, Barbone M, Dumcenco D, Marinov K, et al. High Responsivity, Large-Area Graphene/ MoS_2 Flexible Photodetectors. *ACS Nano*. 2016; 10:8252–8262. [PubMed: 27537529]
12. Lopez-Sanchez O, Lembke D, Kayci M, Radenovic A, Kis A. Ultrasensitive Photodetectors Based on Monolayer MoS_2 . *Nat Nanotechnol*. 2013; 8:497–501. [PubMed: 23748194]
13. Xie X, Ao Z, Su D, Zhang J, Wang G. MoS_2 /Graphene Composite Anodes with Enhanced Performance for Sodium-Ion Batteries: The Role of the Two-Dimensional Heterointerface. *Adv Funct Mater*. 2015; 25:1393–1403.
14. Smolyanitsky A, Yakobson BI, Wassenaar TA, Paulechka E, Kroenlein K. A MoS_2 -Based Capacitive Displacement Sensor for DNA Sequencing. *ACS Nano*. 2016
15. Zhu C, Zeng Z, Li H, Li F, Fan C, Zhang H. Single-Layer MoS_2 -Based Nanoprobes for Homogeneous Detection of Biomolecules. *J Am Chem Soc*. 2013; 135:5998–6001. [PubMed: 23570230]

16. Wang F, Wang Z, Xu K, Wang F, Wang Q, Huang Y, Yin L, He J. Tunable GaTe-MoS₂ van Der Waals P-n Junctions with Novel Optoelectronic Performance. *Nano Lett.* 2015; 15:7558–7566. [PubMed: 26469092]
17. Lee G-H, Yu Y-J, Cui X, Petrone N, Lee C-H, Choi MS, Lee D-Y, Lee C, Yoo WJ, Watanabe K, et al. Flexible and Transparent MoS₂ Field-Effect Transistors on Hexagonal Boron Nitride-Graphene Heterostructures. *ACS Nano.* 2013; 7:7931–7936. [PubMed: 23924287]
18. Laskar MR, Nath DN, Ma L, Li EWL, Lee CH, Kent T, Yang Z, Mishra R, Roldan MA, Idrobo J-C, et al. P-Type Doping of MoS₂ Thin Films Using Nb. *Appl Phys Lett.* 2014; 104:092104.
19. Zhang K, Feng S, Wang J, Azcatl A, Lu N, Addou R, Wang N, Zhou C, Lerach J, Bojan V, et al. Manganese Doping of Monolayer MoS₂: The Substrate Is Critical. *Nano Lett.* 2015; 15:6586–6591. [PubMed: 26349430]
20. Tarasov A, Zhang S, Tsai M-Y, Campbell PM, Graham S, Barlow S, Marder SR, Vogel EM. Controlled Doping of Large-Area Trilayer MoS₂ with Molecular Reductants and Oxidants. *Adv Mater.* 2015; 27:1175–1181. [PubMed: 25580926]
21. Gao J, Kim YD, Liang L, Idrobo JC, Chow P, Tan J, Li B, Li L, Sumpter BG, Lu T-M, et al. Transition-Metal Substitution Doping in Synthetic Atomically Thin Semiconductors. *Adv Mater.* 2016; 28:9735–9743. [PubMed: 27646967]
22. Komsa H-P, Krasheninnikov AV. Two-Dimensional Transition Metal Dichalcogenide Alloys: Stability and Electronic Properties. *J Phys Chem Lett.* 2012; 3:3652–3656. [PubMed: 26291001]
23. Esmaeili-Rad MR, Salahuddin S. High Performance Molybdenum Disulfide Amorphous Silicon Heterojunction Photodetector. *Sci Rep.* 2013; 3
24. Deng Y, Luo Z, Conrad NJ, Liu H, Gong Y, Najmaei S, Ajayan PM, Lou J, Xu X, Ye PD. Black Phosphorus-Monolayer MoS₂ van Der Waals Heterojunction P-n Diode. *ACS Nano.* 2014; 8:8292–8299. [PubMed: 25019534]
25. Ruzmetov D, Zhang K, Stan G, Kalanyan B, Bhimanapati GR, Eichfeld SM, Burke RA, Shah PB, O'Regan TP, Crowne FJ, et al. Vertical 2D/3D Semiconductor Heterostructures Based on Epitaxial Molybdenum Disulfide and Gallium Nitride. *ACS Nano.* 2016; 10:3580–3588. [PubMed: 26866442]
26. Ubaldini A, Jacimovic J, Ubrig N, Giannini E. Chloride-Driven Chemical Vapor Transport Method for Crystal Growth of Transition Metal Dichalcogenides. *Cryst Growth Des.* 2013; 13:4453–4459.
27. Hu T, Bian K, Tai G, Zeng T, Wang X, Huang X, Xiong K, Zhu K. Oxidation-Sulfidation Approach for Vertically Growing MoS₂ Nanofilms Catalysts on Molybdenum Foils as Efficient HER Catalysts. *J Phys Chem C.* 2016; 120:25843–25850.
28. Tai G, Zeng T, Yu J, Zhou J, You Y, Wang X, Wu H, Sun X, Hu T, Guo W. Fast and Large-Area Growth of Uniform MoS₂ Monolayers on Molybdenum Foils. *Nanoscale.* 2016; 8:2234–2241. [PubMed: 26743938]
29. Zhan Y, Liu Z, Najmaei S, Ajayan PM, Lou J. Large-Area Vapor-Phase Growth and Characterization of MoS₂ Atomic Layers on a SiO₂ Substrate. *Small.* 2012; 8:966–971. [PubMed: 22334392]
30. Lee Y-H, Yu L, Wang H, Fang W, Ling X, Shi Y, Lin C-T, Huang J-K, Chang M-T, Chang C-S, et al. Synthesis and Transfer of Single-Layer Transition Metal Disulfides on Diverse Surfaces. *Nano Lett.* 2013; 13:1852–1857. [PubMed: 23506011]
31. Rong Y, Fan Y, Koh AL, Robertson AW, He K, Wang S, Tan H, Sinclair R, Warner JH. Controlling Sulphur Precursor Addition for Large Single Crystal Domains of WS₂. *Nanoscale.* 2014; 6:12096–12103. [PubMed: 25195869]
32. Xia J, Huang X, Liu L-Z, Wang M, Wang L, Huang B, Zhu D-D, Li J-J, Gu C-Z, Meng X-M. CVD Synthesis of Large-Area, Highly Crystalline MoSe₂ Atomic Layers on Diverse Substrates and Application to Photodetectors. *Nanoscale.* 2014; 6:8949–8955. [PubMed: 24965908]
33. Zhou L, Xu K, Zubair A, Liao AD, Fang W, Ouyang F, Lee Y-H, Ueno K, Saito R, Palacios T, et al. Large-Area Synthesis of High-Quality Uniform Few-Layer MoTe₂. *J Am Chem Soc.* 2015; 137:11892–11895. [PubMed: 26305492]
34. Keyshar K, Gong Y, Ye G, Brunetto G, Zhou W, Cole DP, Hackenberg K, He Y, Machado L, Kabbani M, et al. Chemical Vapor Deposition of Monolayer Rhenium Disulfide (ReS₂). *Adv Mater.* 2015; 27:4640–4648. [PubMed: 26140355]

35. Yu Y, Li C, Liu Y, Su L, Zhang Y, Cao L. Controlled Scalable Synthesis of Uniform, High-Quality Monolayer and Few-Layer MoS₂ Films. *Sci Rep.* 2013; 3:1866. [PubMed: 23689610]
36. Kang K, Xie S, Huang L, Han Y, Huang PY, Mak KF, Kim C-J, Muller D, Park J. High-Mobility Three-Atom-Thick Semiconducting Films with Wafer-Scale Homogeneity. *Nature.* 2015; 520:656–660. [PubMed: 25925478]
37. Tan LK, Liu B, Teng JH, Guo S, Low HY, Loh KP. Atomic Layer Deposition of a MoS₂ Film. *Nanoscale.* 2014; 6:10584–10588. [PubMed: 25069589]
38. Groven B, Heyne M, Nalin Mehta A, Bender H, Nuytten T, Meersschant J, Conard T, Verdonck P, Van Elshocht S, Vandervorst W, et al. Plasma-Enhanced Atomic Layer Deposition of Two-Dimensional WS₂ from WF₆, H₂ Plasma, and H₂S. *Chem Mater.* 2017; 29:2927–2938.
39. Eichfeld SM, Hossain L, Lin Y-C, Piasecki AF, Kupp B, Birdwell AG, Burke RA, Lu N, Peng X, Li J, et al. Highly Scalable, Atomically Thin WSe₂ Grown via Metal–Organic Chemical Vapor Deposition. *ACS Nano.* 2015; 9:2080–2087. [PubMed: 25625184]
40. Jones, AC., Hitchman, ML., editors. *Chemical Vapour Deposition: Precursors, Processes and Applications.* Royal Society of Chemistry; Cambridge, UK: 2009.
41. Ludlum KH, Eischens RP. Carbonyl Formation in Stainless Steel Infrared Cells. *Surf Sci.* 1973; 40:397–398.
42. Salzer A. Nomenclature of Organometallic Compounds of the Transition Elements (IUPAC Recommendations 1999). *Pure Appl Chem.* 2009; 71:1557–1585.
43. Garner S, Glaesemann S, Li X. Ultra-Slim Flexible Glass for Roll-to-Roll Electronic Device Fabrication. *Appl Phys A.* 2014; 116:403–407.
44. Kimes WA, Moore EF, Maslar JE. Perpendicular-Flow, Single-Wafer Atomic Layer Deposition Reactor Chamber Design for Use with in Situ Diagnostics. *Rev Sci Instrum.* 2012; 83:083106. [PubMed: 22938273]
45. Ganta D, Sinha S, Haasch RT. 2-D Material Molybdenum Disulfide Analyzed by XPS. *Surf Sci Spectra.* 2014; 21:19–27.
46. Powell, CJ., Jablonski, A. NIST Electron Inelastic-Mean-Free-Path Database. National Institute of Standards and Technology; Gaithersburg, MD: 2010. Vol. Version 12
47. Haynes, WM. *CRC Handbook of Chemistry and Physics.* 97th. CRC Press; Boca Raton, FL: 2016. Physical Constants of Inorganic Compounds; p. 4-75.
48. Benameur MM, Radisavljevic B, Héron JS, Sahoo S, Berger H, Kis A. Visibility of Dichalcogenide Nanolayers. *Nanotechnology.* 2011; 22:125706. [PubMed: 21317494]
49. Bertuch A, Sundaram G, Saly M, Moser D, Kanjolia R. Atomic Layer Deposition of Molybdenum Oxide Using Bis(tert-Butylimido)bis(dimethylamido) Molybdenum. *J Vac Sci Technol A.* 2014; 32:01A119.
50. Miikkulainen V, Suvanto M, Pakkanen TA. Bis(tert-Butylimido)-Bis(dialkylamido) Complexes of Molybdenum as Atomic Layer Deposition (ALD) Precursors for Molybdenum Nitride: The Effect of the Alkyl Group. *Chem Vap Depos.* 2008; 14:71–77.
51. Miikkulainen V, Suvanto M, Pakkanen TA. Atomic Layer Deposition of Molybdenum Nitride from Bis(tert-Butylimido)-Bis(dimethylamido)molybdenum and Ammonia onto Several Types of Substrate Materials with Equal Growth per Cycle. *Chem Mater.* 2007; 19:263–269.
52. Serna MI, Yoo SH, Moreno S, Xi Y, Oviedo JP, Choi H, Alshareef HN, Kim MJ, Minary-Jolandan M, Quevedo-Lopez MA. Large-Area Deposition of MoS₂ by Pulsed Laser Deposition with In Situ Thickness Control. *ACS Nano.* 2016; 10:6054–6061. [PubMed: 27219117]
53. Li H, Zhang Q, Yap CCR, Tay BK, Edwin THT, Olivier A, Baillargeat D. From Bulk to Monolayer MoS₂: Evolution of Raman Scattering. *Adv Funct Mater.* 2012; 22:1385–1390.
54. Li S-L, Miyazaki H, Song H, Kuramochi H, Nakaharai S, Tsukagoshi K. Quantitative Raman Spectrum and Reliable Thickness Identification for Atomic Layers on Insulating Substrates. *ACS Nano.* 2012; 6:7381–7388. [PubMed: 22838842]
55. Eda G, Yamaguchi H, Voiry D, Fujita T, Chen M, Chhowalla M. Photoluminescence from Chemically Exfoliated MoS₂. *Nano Lett.* 2011; 11:5111–5116. [PubMed: 22035145]
56. Li W, Birdwell AG, Amani M, Burke RA, Ling X, Lee Y-H, Liang X, Peng L, Richter CA, Kong J, et al. Broadband Optical Properties of Large-Area Monolayer CVD Molybdenum Disulfide. *Phys Rev B.* 2014; 90:195434.

57. Park JW, So HS, Kim S, Choi S-H, Lee H, Lee J, Lee C, Kim Y. Optical Properties of Large-Area Ultrathin MoS₂ Films: Evolution from a Single Layer to Multilayers. *J Appl Phys.* 2014; 116:183509.
58. Gao J, Li B, Tan J, Chow P, Lu T-M, Koratkar N. Aging of Transition Metal Dichalcogenide Monolayers. *ACS Nano.* 2016; 10:2628–2635. [PubMed: 26808328]
59. Hahn, T., editor. *International Tables for Crystallography: Space-Group Symmetry*. 1st. International Union of Crystallography; Chester, England: 2006. *International Tables for Crystallography* Vol. A
60. Schönfeld B, Huang JJ, Moss SC. Anisotropic Mean-Square Displacements (MSD) in Single-Crystals of 2H- and 3R-MoS₂. *Acta Crystallogr B.* 1983; 39:404–407.
61. Wang S, Zhang J, He D, Zhang Y, Wang L, Xu H, Wen X, Ge H, Zhao Y. Sulfur-Catalyzed Phase Transition in MoS₂ under High Pressure and Temperature. *J Phys Chem Solids.* 2014; 75:100–104.
62. Addou R, Colombo L, Wallace RM. Surface Defects on Natural MoS₂. *ACS Appl Mater Interfaces.* 2015; 7:11921–11929. [PubMed: 25980312]
63. Baker MA, Gilmore R, Lenardi C, Gissler W. XPS Investigation of Preferential Sputtering of S from MoS₂ and Determination of MoS_x Stoichiometry from Mo and S Peak Positions. *Appl Surf Sci.* 1999; 150:255–262.
64. Zhu H, Qin X, Cheng L, Azcatl A, Kim J, Wallace RM. Remote Plasma Oxidation and Atomic Layer Etching of MoS₂. *ACS Appl Mater Interfaces.* 2016; 8:19119–19126. [PubMed: 27386734]
65. Fix R, Gordon RG, Hoffman DM. Low-Temperature Atmospheric-Pressure Metal-Organic Chemical Vapor Deposition of Molybdenum Nitride Thin Films. *Thin Solid Films.* 1996; 288:116–119.
66. Estrade-Szwarckopf H. XPS Photoemission in Carbonaceous Materials: A “defect” Peak beside the Graphitic Asymmetric Peak. *Carbon.* 2004; 42:1713–1721.
67. Jiang Z, Huang W, Zhang Z, Zhao H, Tan D, Bao X. Thermal Decomposition of Mo(CO)₆ on Thin Al₂O₃ Film: A Combinatorial Investigation by XPS and UPS. *Surf Sci.* 2007; 601:844–851.
68. Hofmann WK. Thin Films of Molybdenum and Tungsten Disulphides by Metal Organic Chemical Vapour Deposition. *J Mater Sci.* 1988; 23:3981–3986.

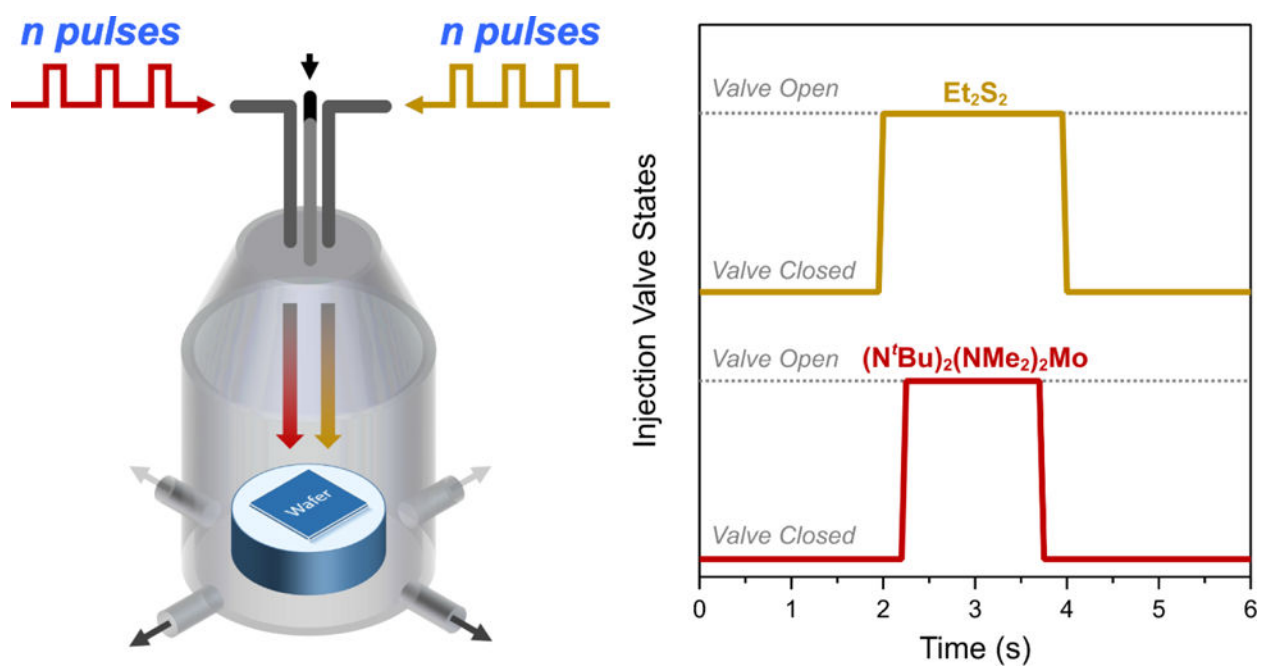


Figure 1. Overview of the pulsed MOCVD process. A schematic of the reactor geometry is shown on the right and the injection sequence of the Mo and S precursors in a 6 s period is shown on the left.

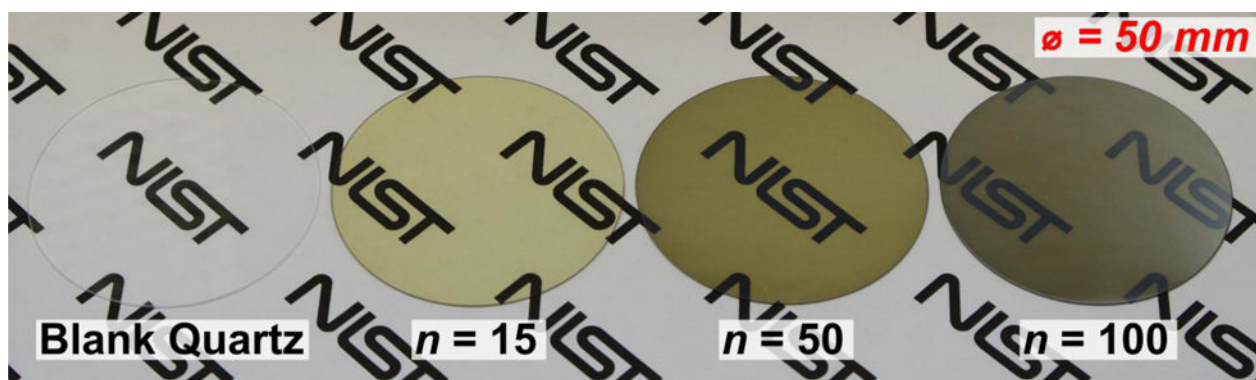


Figure 2. Photographs of 50 mm diameter fused quartz wafers demonstrate wafer-scale growth of MoS₂. Left to right: a blank wafer and wafers with MoS₂ deposited with varying numbers of pulses. Logo that appears in the background used with permission of the National Institute of Standards and Technology (NIST).

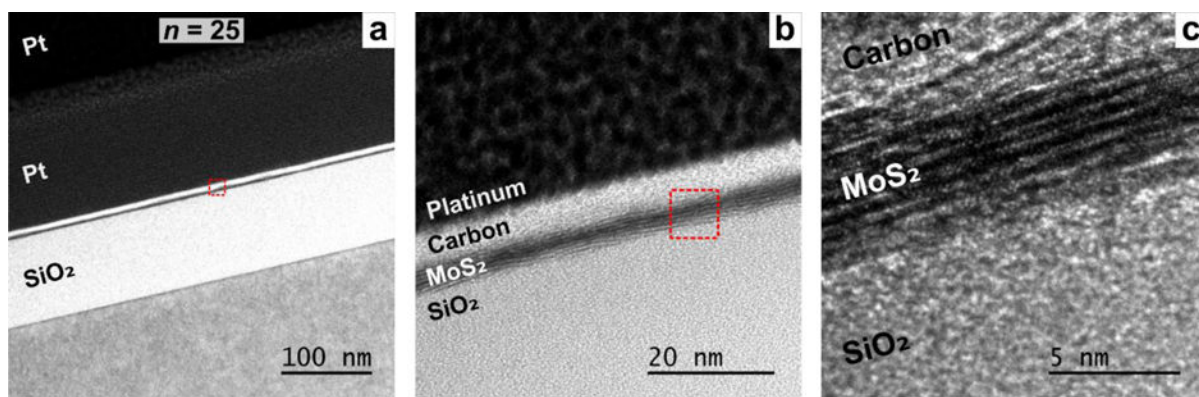


Figure 3. HRTEM cross sections from MOCVD grown MoS₂ on SiO₂/Si shown at (a) low, (b) medium, and (c) high magnification.

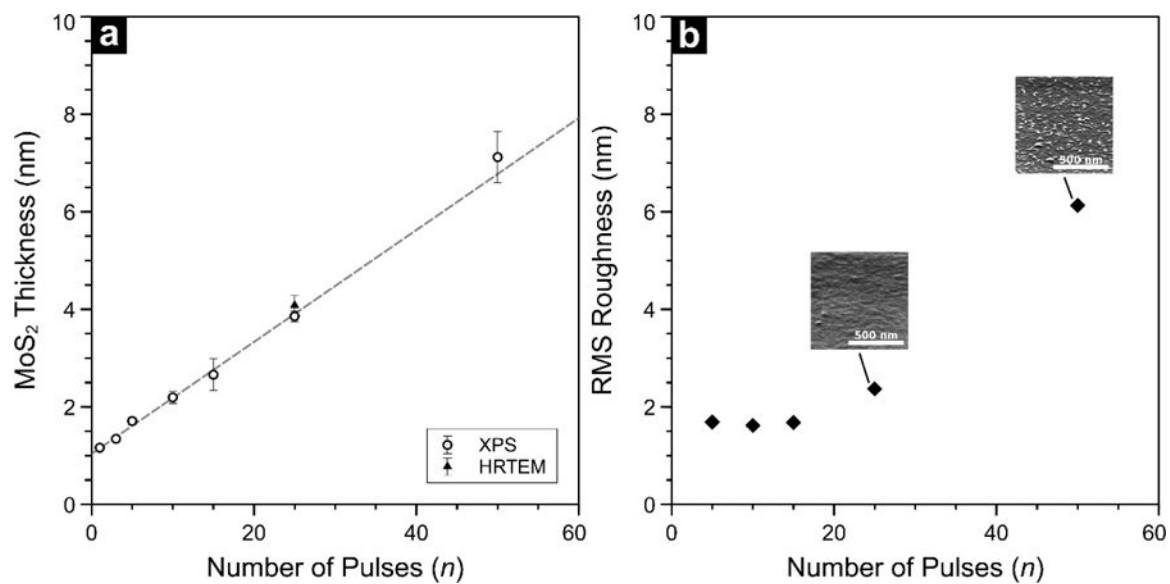


Figure 4.

In (a), film thickness estimated from Si 2p photoelectron attenuation is plotted as a function of pulse count. Error bars represent one standard deviation of the mean. (b) Shows root mean square surface roughness as determined by AFM. Inset panels in (b) show perspective view (70° tilt) SEM images for 25 and 50 pulses.

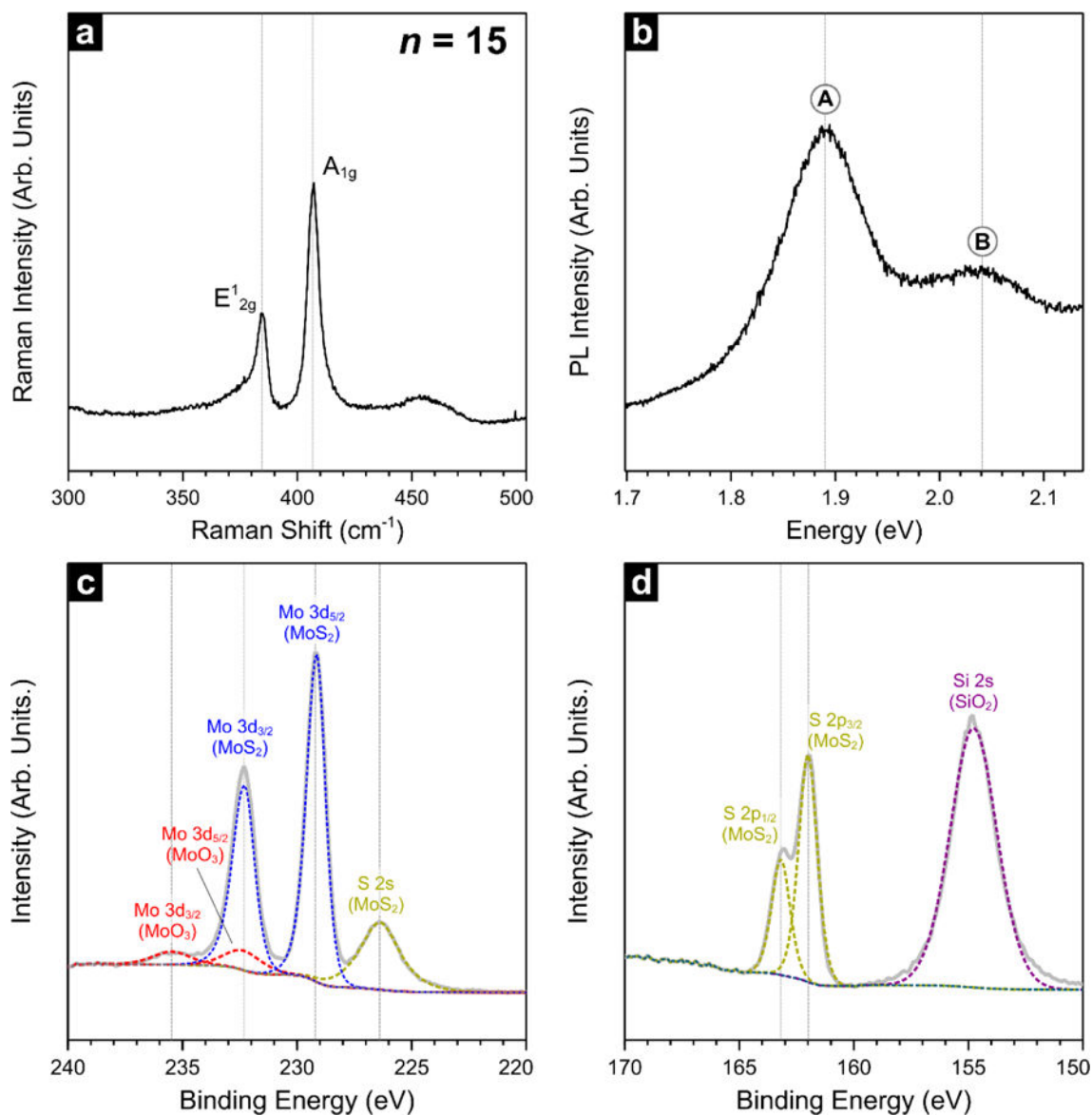


Figure 5. Raman (a) and PL (b) spectra for a few-layer MOCVD MoS₂ film ($n=15$) deposited on SiO₂. X-ray photoelectron spectra from the same surfaces are shown for the Mo 3d region in (c) and the S 2p region in (d).

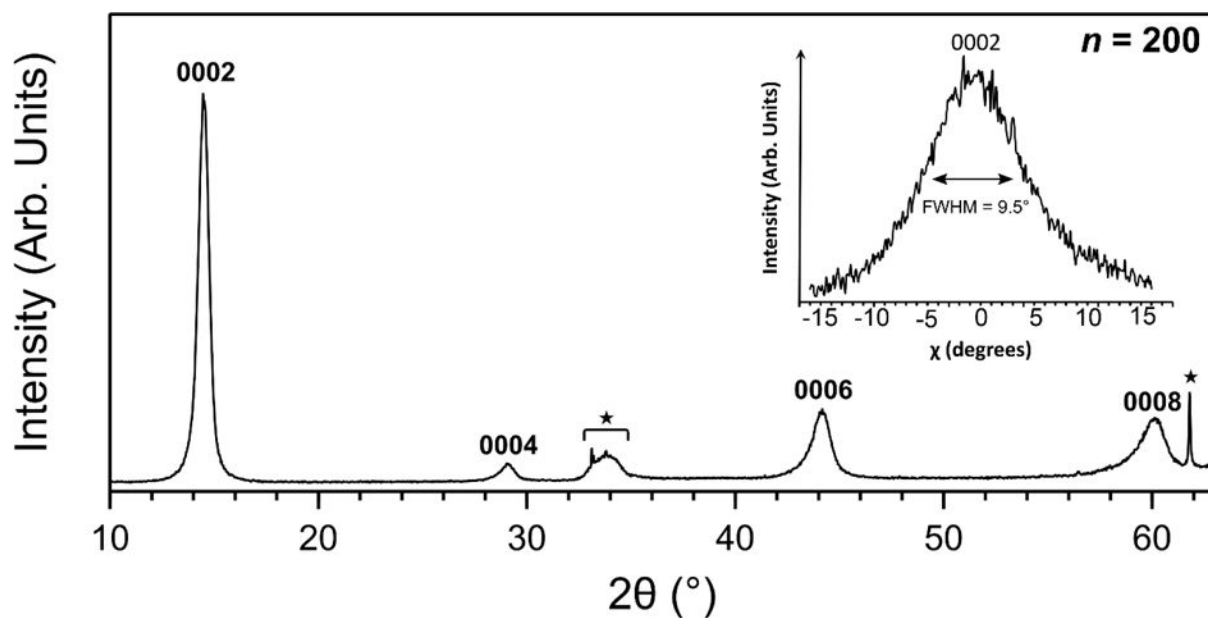


Figure 6. θ - 2θ XRD scans from a thick MoS₂ films (≈ 25 nm, $n=200$) grown at 591 °C. Absence of the hkl reflections other than from the {0002} family is evidence for 0002 texture in the film. A high degree of texture is also evident from a relatively narrow rocking curve shown in the inset, which shows an integrated intensity for the 0002 reflection vs χ -angle produced from the XRD² diffraction (not shown). Reflections identified with a star (★) on the θ - 2θ scan are from the Si (100) substrate. The lattice parameter is calculated as $c = 1.2306(5)$ nm.

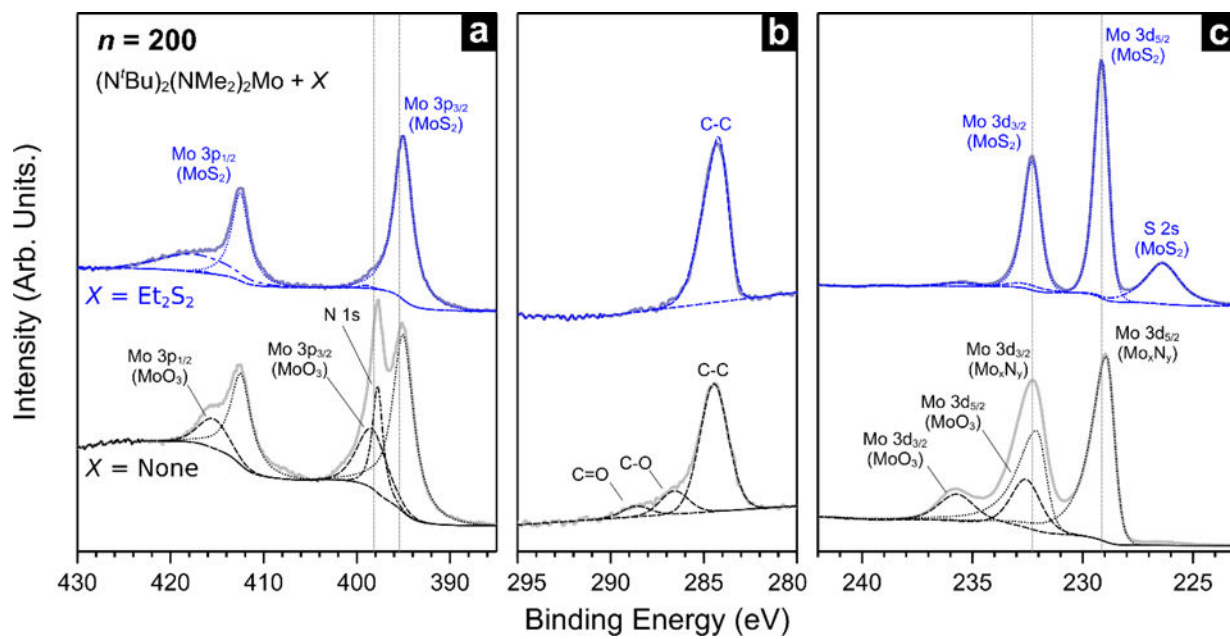


Figure 7. High resolution XPS spectra and synthetic peak fitting in the Mo 3p (a), C 1s (b), and Mo 3d (c) core levels from films prepared using $n=200$ pulses with ($X=Et_2S_2$) and without ($X=None$) a sulfur co-reactant.